Mon. Not. R. Astron. Soc. **000**, 000–000 (0000) Printed 19 August 2011 (MN LaTeX style file v2.2)

The dynamics and environmental impact of 3C 452

D.L. Shelton[1]∗, M.J. Hardcastle[1] and J.H. Croston[2]
[1] *School of Physics, Astronomy & Mathematics, University of Hertfordshire, College Lane, Hatfield, AL10 9AB*
[2] *School of Physics and Astronomy, University of Southampton, Southampton, Hampshire, SO17 1BJ*

arXiv:1108.3753v1 [astro-ph.CO] 18 Aug 2011

19 August 2011

ABSTRACT
We present a detailed analysis of a new *XMM-Newton* observation of the FRII radio galaxy 3C 452 and its environment. We detect X-ray emission from the hot intragroup medium and measure its temperature as well as obtaining the surface brightness and pressure profiles. We provide evidence that 3C 452 is currently heating its environment, measuring a temperature of 1.18 ± 0.11 keV for the immediate environment of the radio source compared to $0.86^{+0.13}_{-0.05}$ keV for the outer environment) . We also present evidence that the outer regions of the lobes are overpressured (internal pressure of 2.6×10^{-13} Pa and external pressure of $1.11 \pm 0.11 \times 10^{-13}$ Pa at the edge of the lobes) and therefore are driving a shock at the lobe edges (with a temperature which we constrain to be $1.7^{+0.9}_{-0.5}$ keV), while the inner regions of the lobes are underpressured and contracting. Taking into account the very large amount of energy stored in the lobes, we show that this relatively low-powered FRII radio galaxy will have an extremely significant impact on its group environment.

Key words: galaxies: active – galaxies: individual (3C 452) – galaxies: ISM – X-rays: galaxies

1 INTRODUCTION

Understanding how a powerful radio galaxy interacts with a poor environment is important in exploring the impact of radio galaxies on the properties of the group population. The most powerful class of jet-driven AGN outbursts that we know of are the FRII radio galaxies (Fanaroff & Riley 1974). X-ray observations of some of these objects suggest that the energy input from the expanding radio galaxy can be similar to the binding energy of the local intergalactic medium (e.g. Kraft et al. 2007, Hardcastle et al. 2007a); thus it is clear that in principle those sources will have a profound effect on their environments over their lifetimes.

The radio lobes in FRII radio galaxies are the result of the interactions between the relativistic electrons that have passed up the jet and the external medium, where the electrons gain energy at the jet termination shocks and expand out into the external medium (Scheuer 1974). It has been known for many years that the inflation of these lobes should affect the surrounding intergalactic medium (IGM). Even when the lobes expand at sub-sonic speeds (where the internal lobe and ram pressures are comparable to the external pressure), they do $p\mathrm{d}V$ work on the hot gas. When the lobes expand at supersonic speeds, we expect additional work to be done to shock-heat the gas. This is a non-adiabatic process that effects the entropy as well as the internal energy of the external medium.

However, it is only recently that we have been able to make detailed statements about the internal and external pressures of FRII radio galaxies in typical environments, which determine their dynamics. This change has come about because the current generation of X-ray telescopes, *XMM-Newton* and *Chandra*, have the ability to detect inverse-Compton emission from the lobes together with thermal emission from their hot gas environments, which are often relatively poor (Croston et al. 2004; Kraft et al. 2007; Hardcastle et al. 2007b; Belsole et al. 2007). Detection and characterization of these X-ray components allows us to describe the current dynamics of the radio lobes and gives us some idea what the energy input to the external environment over the lifetime of the radio source must have been. The impact that the AGN outbursts have on the hot IGM has implications for the history and evolution of the hot phase of the baryonic matter and the nature of 'feedback' from radio-loud active galaxies. When discussing the evolution of hot gas, it is important to understand that, although powerful radio-loud AGN are rare, their impact can be long lived: a single FRII outburst can have an effect on the IGM surrounding the AGN galaxy that exceeds that of a large number of less violent, longer-lived low-power radio sources (Basson & Alexander 2003) and many groups that no longer show signs of AGN may once have hosted FRII sources.

Detailed studies of the dynamics of radio galaxies using X-ray observations rely on the capability of separating the thermal and non-thermal emission from the source. Some of the non-thermal emission comes in the form of synchroton and inverse-Compton emission from the jets and hotspots, which is generally best studied at high resolution with *Chandra*. However, the dominant non-thermal component in powerful radio galaxies is inverse-Compton emission from the lobes. This occurs when electrons in the lobes scatter cosmic microwave background (CMB) photons to X-ray energies (e.g. Feigelson et al. 1995; Tashiro et al. 1998

∗ E-mail:D.Shelton@herts.ac.uk

Hardcastle et al. 2002; Kataoka & Stawarz 2005; Croston et al. 2005b). To be able to separate the non-thermal and thermal components, we need to study objects where we can obtain a significant number of counts from both the lobes and the thermal environment. In particular, to avoid the inverse-Compton emission being dominated by thermal bremsstrahlung (cf. Hardcastle & Croston (2010)) we need to select objects that are powerful, close and inhabit relatively poor environments.

In this paper we study the nearby, powerful radio galaxy 3C452. 3C452 is an FRII radio galaxy which has a symmetrical double-lobe morphology and a relatively uniform surface brightness distribution (Black et al. 1992); its largest angular size is ~ 5 arcmin, which at its redshift of 0.0811 corresponds to a projected linear size of ~ 450 kpc. Images from the *Hubble Space Telescope* and various sky surveys (such as 2MASS) suggest that the environment is a poor group, with a clear excess of galaxies within the instrument's field of view; however, group membership has not been confirmed spectroscopically for any of the nearby galaxies.

Isobe et al. (2002) discussed *Chandra* observations of 3C 452, showing that there is clear inverse-Compton emission from the lobes. However, their observations were not sensitive enough to make measurements of the properties of any extended thermal environment. In this paper we describe the results of a deep *XMM-Newton* observation of 3C452. *XMM-Newton's* higher sensitivity and larger field of view when compared to *Chandra* allow us to detect and constrain the properties of the group-scale gas around 3C452 and to search for evidence both for shock heating and for other work done on the external medium by the radio galaxy.

In the cosmology used in this thesis, the luminosity distance to 3C452 is 369 Mpc, and 1 arcsec corresponds to 1.53 kpc. Errors quoted on the results of X-ray fitting are 90 per cent confidence errors.

2 OBSERVATION & DATA REDUCTION

We observed 3C452 with the EPIC instrument on board *XMM-Newton*. The exposure time for the MOS1 and MOS2 cameras were 69.587 ks and 69.621 ks respectively. For the PN, the exposure time was 54.024 ks. The observation began on 2008 November 30.

The datasets were processed using the Scientific Analysis Software (SAS) version 9.0 and the standard pipeline tasks *emchain* and *epchain*. The data was filtered using PATTERN $<= 4$ (MOS) or PATTERN $<= 12$ (PN) and we used the bit-mask flags 0x766a0600 for the MOS camera and 0xfa000c for the PN camera. These are equivalent to the standard flagset #XMMEA_EM/P, but they also include out of field-of-view events and exclude any bad columns and rows found in the data. We did not need to filter the data in the time domain, as there were not any background flares in the dataset. The dataset was also energy filtered between 0.2 and 12 keV for the MOS cameras and between 0.2 and 15 keV for the PN camera, using *xmmselect*. We then used *evigweight* to apply a vignetting correction to the files and extracted spectra from each camera using *evselect*. *Evigweight* is a standard SAS tool which properly propagates statistical errors. We use the SAS tool *arfgen* to create the ancillary response files. Vignetting is not taken into account when creating the ancillary reponse files as it is already accounted for by the weighting factor applied by *evigweight*.

In order to identify suitable regions for spectral analysis, it is first necessary to create an image. We used *xmmselect* to create an image for each camera in the 0.3–8 keV energy band, and then combined these images to generate an exposure map for each camera to correct for chip gaps.

We used a *Chandra* observation, first described by Isobe et al. (2002), to identify point sources in the image. These were then removed from the combined image and Gaussian smoothing was used. We experimented with a range of kernel sizes so structure could be emphasized on different size scales (see Fig. 1). Figure 2 shows the X-ray emission from the lobes of 3C 452.

Finally, we made use of a radio map of 3C 452 from the online 3CRR Atlas[1], at a frequency of 1.4 GHz and with a resolution of 6 arcsec.

3 SPECTROSCOPIC ANALYSIS

In this section we discuss the two methods we used to extract spectra for the various components of the radio galaxy and its environment and then go on to discuss our results. Throughout the spectroscopic analysis, we used events in the energy range 0.3 – 8 keV.

3.1 Background methods

We used two approaches to determining the appropriate background for our spectra: local background regions and a full double-subtraction technique that takes account of the spatially variable particle background. Where possible we used a local background for simplicity. However, doing this for regions over which the particle background might be spatially variable leads to bias in the results, and so for larger regions we used closed-filter data with instrument modes matching our observations to constrain the particle background properties. In this situation, we used the method of Maurin et al. (in prep); which is described by Croston et al. (2008). As in Croston et al. (2008), we calculated particle background scaling factors by comparing the 10–12 keV (MOS) and 12–14 keV (PN) count rates for the source and closed-filter datasets[2]. The exposure times for the data sets were 107 ks for MOS1, 83 ks for MOS2 and 196 ks for PN. We used a circular region with a radius of 12,000 pixels in the energy ranges stated above. After this we extracted spectra for the source files and the background files and measured the count rate. Our scaling factors (ratio between the count rate of the source files and the count rate for the closed filter files) for the MOS1, MOS2 and PN cameras are 1.54, 1.70 and 1.63 respectively.

We chose a background region which was near the source, but did not contain any emission from it (this region lies between 320 and 480 arcseconds from the source as shown in Section 3.2) The spectra for the X-ray background for the three cameras, determined from this background region, were then modelled in XSPEC, ignoring the energy range between 1.4 and 1.6 keV where an instrumental line affects the fit. The X-ray background is modelled as a double *apec* + absorbed power law, with the column density fixed to the Galactic value and abundance fixed at solar. The two *apec* models account for the emission from the Galactic bubble and the power law accounts for the cosmic X-ray background. The temperatures were allowed to vary, as were the normalizations, but the power law index was fixed at $\Gamma = 1.41$ (Lumb et al. 2002). The normalizations were allowed to vary to help minimize intrumental differences between the MOS and PN cameras and to account for

[1] http://www.jb.man.ac.uk/atlas/

[2] http://xmm2.esac.esa.int/external/xmm_sw_cal/background/filter_closed/index.shtml

differences in the local X-ray background in different directions. Finally, a scaled version of this spectrum, with all parameters fixed, was used in fits to the spectra for each source region. Table 1 shows the parameters of the best-fitting model for the background region we used. Our model is in agreement with the model of Lumb et al. (2002).

3.2 Regions for spectral extraction

We extracted spectra for the following regions:

(i) An inner region (radius 160 arcsec) surrounding the source (region 1 in Fig. 1)
(ii) An outer annulus (radii between 160 and 320 arcsec: region 2 in Fig. 1)
(iii) A region just outside the end of the E lobe (region 3 in Fig. 1)
(iv) A blank-sky region for use in the double subtraction method (an annulus between 320 and 480 arcsec as described in section 3.1,(region 4 in Fig. 1).
(v) The background region used for region 3 (region 5).
(vi) The AGN and lobes

We extracted the AGN spectrum by taking a circular region with a radius of 25 arcsec (38.25 kpc) around the AGN and used a local annulus with a radius of 59 arcsec (90.27 kpc) for the background. We also excluded a 12 arcsec (18.36 kpc) region to the North-East of the AGN to remove a point source that would have affected our results. The same method was used for the lobes, but instead of a circular region, we took a rectangular region of length 247 arcsec (378 kpc) by 130 arcsec (199 kpc). The regions for the AGN and the region to the North-East of the AGN were excluded as well. We used the double subtraction method to determine the background for this region.

Double subtraction was also used for our two large-scale regions, intended to measure the temperature of group-scale gas which can be detected by eye in heavily smoothed images out to 320 arcsec. Our choice of a 160-arcsec radius (taking the AGN as the centre) boundary between inner and outer regions was intended to separate material that could have been been directly influenced by the radio galaxy from material that should still be in its original undisturbed state. The distance of 160 arcsec just beyond the projected length of one lobe. We masked out point sources seen in the *Chandra* data for these two regions.

Finally, region 3 was a rectangular region just outside the eastern edge of the eastern radio lobe. This rectangle was 111 arcsec in length and 70 arcsec in width. We then took a local circular background region with a 30 arcsec radius. There were no point sources in either region. This region was chosen to allow us to search for any cluster gas that could have been shocked by the radio source. We do not define a corresponding region on the western edge of the source as there is a chip gap on the pn detector that covers the edge of the lobes on that side. For the western lobe we attempted to use a very similar region. However, we were only able to use the MOS cameras for the western lobe and because of this the data quality was poor and we were not able to constrain the temperature.

3.3 Results

In this section we describe the results of spectral fitting to each of the regions described above.

3.3.1 The AGN

The model we used was a model that has been successfully fitted for other NLRGs, consisting of a Galactic absorbed power law together with an intrinsically absorbed power law and an iron Kα line, which gives a very good fit to the data. Parameters of the best-fitting model are given in Table 2. We use a fixed photon index of 2.00 for the soft power-law component following (Hardcastle et al. 2006), since the photon index is poorly determined.

3.3.2 The lobes

To avoid having to mask out a large region, we extracted a spectrum for both the AGN and the lobes together and then fixed the parameters of the AGN model to the best-fitting values found in the analysis of the AGN spectrum (see previous section). We then added to the model a power law to model inverse-Compton emission from the lobes. In addition, we tried the fit both with and without an *apec* model intended to represent thermal emission from the regions in front of and behind the lobes in our extraction region. We found that the fit was marginally improved with the inclusion of an *apec* model with Galactic absorption and abundance fixed at 0.3 solar (χ^2/dof was 1229/1049 with and 1241/1051 without the *apec* model) and so, given that we expect some thermal emission to be present in the extraction region and that this makes our analysis consistent with that of Isobe et al. (2002), we chose to include it in our final fits. We find a photon index for the power-law component of $1.71^{+0.13}_{-0.17}$, and its normalization corresponds to a 1 keV flux density of $39.9^{+4.6}_{-4.1}$ nJy. Parameters for the best-fitting models are given in Table 3. For completeness, we also attempted to model the lobes with an *apec* model alone, but this gave a significantly poorer fit (χ^2/dof of 1650/1051) so we do not consider this model further. The temperature we find for the lobes is consistent within the errors with the temperature we determine for region 1.

3.3.3 Regions outside the lobes

For region 1, we adopted the same approach as described above for the lobes: the spectrum we extracted was for the whole region inside 160 arcsec and we then fixed the parameters of our best-fitting model for the AGN and lobes in the fit. The spectrum for the AGN, lobes and the environment is shown in Figure 3. The spectrum for the outer region (region 4) is shown in Figure 4. The model for the extended emission in this region was an *apec* model with Galactic absorption and abundance fixed to 0.3 solar; we found that a temperature of 1.18 ± 0.11 keV provided a very good fit to the data.

For region 2 we simply fitted an *apec* model with Galactic absorption and abundance fixed to 0.3 solar to the background-subtracted data. We found a best-fitting temperature of $0.86^{+0.13}_{-0.05}$ keV.

Fitting the same *apec* model to the region at the edge of the lobes (region 3) we find a best-fitting temperature of $1.7^{+0.9}_{-0.5}$ keV. Parameters for the best-fitting models of all three regions are given in Table 3.

4 SPATIAL ANALYSIS

4.1 Radial Profiling

To characterize the extended, thermal emission around 3C 452 we generated a radial profile of the X-ray emission in the 0.3 – 8.0

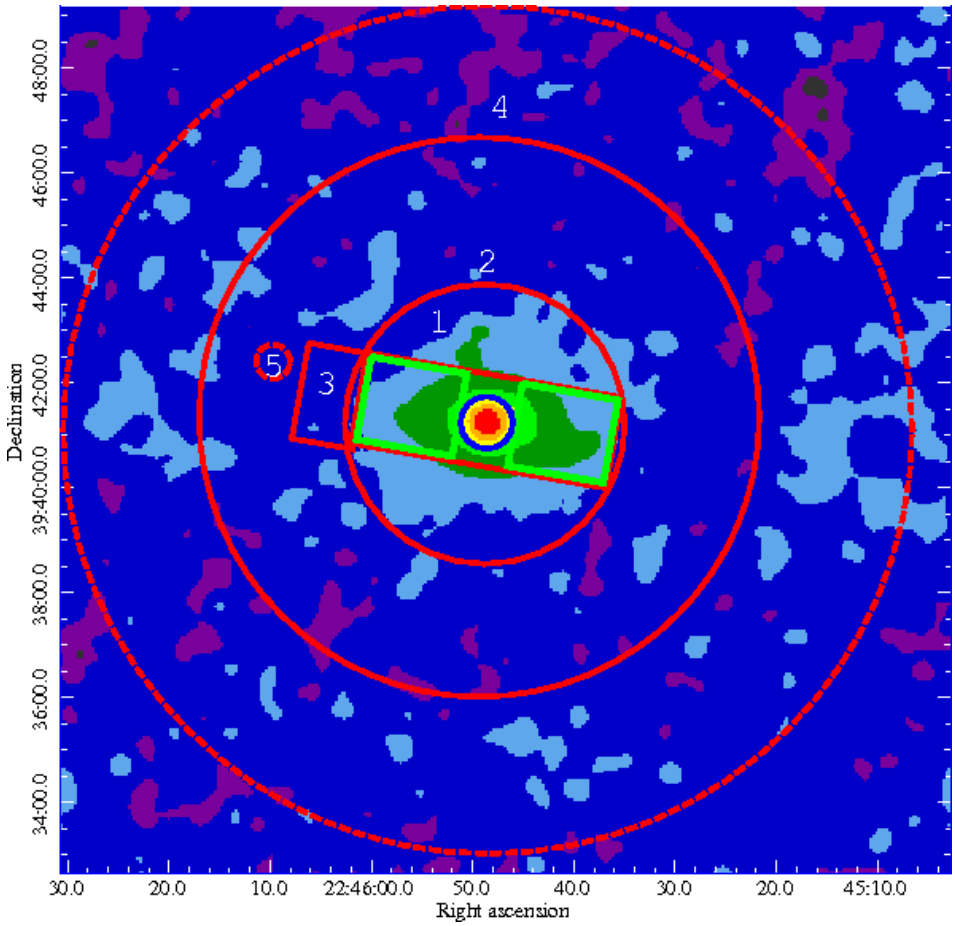

Figure 1. A smoothed image of 3C452 in the energy band 0.3 - 8 keV after the removal of point sources. The image has been binned to 3.2 arcsec per pixel and smoothed with a 2-dimensional Gaussian of $\sigma = 3$ pixels. The image includes contours from the radio map described in Section 2. The contour levels are 0.005, 0.001, 0.05, 0.021 and 0.21 Jy beam^{-1}. The regions described in the text are labelled: 1 for region 1, 2 for region 2 and 3 for region 3, 4 for region 4 and 5 for region 5. The smoothing scale is chosen so as to allow both thermal and lobe related (inverse-Compton) emission to be seen.

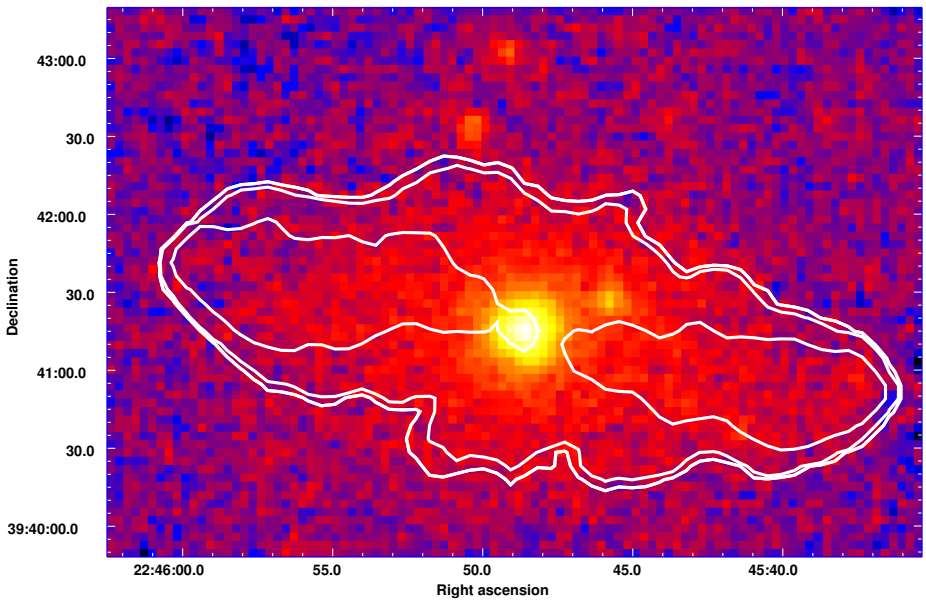

Figure 2. An unsmoothed X-ray image of the AGN and the lobes of 3C 452 in the energy band 0.3-8.0 keV, binned to 3.2 arcsec per pixel. Radio contours are overlaid as in Fig. 1.

Table 1. Best-fitting spectral parameters for the background model; abundance and redshift were fixed values.

Model	Parameter	Value
apec	kT(keV)	$0.055^{+0.012}_{-0.003}$
	Normalization (10^{14} cm^{-5})	$3.05 \pm 1.95 \times 10^{-4}$
	kT(keV)	0.31 ± 0.01
	Normalization (10^{14} cm^{-5})	$2.26^{+0.20}_{-0.37} \times 10^{-5}$
zwabs	nH (10^{22}cm^{-2})	0.1130
powerlaw	Photon Index	1.41
	Normalization (photons keV^{-1} cm^{-2}s^{-1})	$8.08^{+0.37}_{-0.19} \times 10^{-5}$
χ^2/dof	789/468	

Table 2. Best-fitting spectral parameters for the AGN

Model	Parameter	Value
wabs	nH (10^{22}cm^{-2})	0.1130 (fixed)
powerlaw	Photon Index	2.00 (fixed)
	Normalization (photons keV^{-1} cm^{-2}s^{-1})	$1.03^{+0.03}_{-0.26} \times 10^{-4}$
zwabs	nH (10^{22}cm^{-2})	$43.59^{+5.27}_{-4.37}$
	Redshift	0.0811
powerlaw	Photon index	$1.26^{+0.32}_{-0.27}$
	Normalization (photons keV^{-1} cm^{-2}s^{-1})	$6.42^{+9.33}_{-2.19} \times 10^{-4}$
Gaussian	E(keV)	6.42 ± 0.02
	σ	0.08 ± 0.03
	Normalization (photons cm^{-2} s^{-1})	$1.76^{+0.35}_{-0.32} \times 10^{-5}$
Unabsorbed 0.5 - 10 keV luminosity (ergs s^{-1}):	$(1.02 \pm 0.2) \times 10^{44}$	
χ^2/dof	1252/1058	

keV band. We binned the data adaptively to give a similar signal-to-noise ratio in each radial bin. We masked out the lobe regions to avoid any contribution from inverse-Compton emission to the radial profile, but the AGN was not masked out. We were able to do this by using two boxes to exclude the lobes as shown by the green boxes in Figure 1.

The particle background was modelled using the closed-filter images described in Section 3.1. The files were vignetting-corrected and filtered in the same way as the 3C 452 observations and were rotated to be at the same angle as the dataset using the SAS task *attcalc*. Using the scaling factors described in Section 3.1, we were then able to subtract a position-dependent background correction from each radial bin. The X-ray background contribution was subtracted using the outermost annulus of our profile (region 4 in figure 1) Finally, the radial profiles for each camera were combined to produce a profile of net count rate per unit area.

We then fitted a model consisting of a point source, with free normalization, and a β model with free β, core radius and normalization to the radial profile. Each component of the model was convolved with an *XMM-Newton* point spread function derived from the combined point-spread functions of the three cameras, suitably weighted. The fitting process used a Markov-Chain Monte-Carlo algorithm described in detail in Goodger et al. (2011), an updated version of the method used by Croston et al. (2008).

The best-fitting β model, ($\chi^2/\mathrm{dof} = 66/9$) has $\beta = 0.53 \pm 0.02$ and the core radius was 21.98 ± 1.05 arcsec. Figure 5 shows the surface brightness profile with the best-fitting model. Although it would have been possible to fit more complex models (e.g. a double β model as used by Croston et al. 2005b) to the data, our aim was just to characterise the density and pressure profiles in the inner regions and this simple model provides an adequate representation of the data here.

The surface brightness profile presented in Figure 5 takes into account only the statistical uncertainty in surface brightness based on the count levels in the source and background annulus region. It is important also to consider any systematic uncertainty introduced by the use of the filter-wheel closed (FWC) background files in the double-subtraction process. The particle background scaling factors have a small associated uncertainty from the target observation and background file high-energy count rates used to determine the scaling; however, the dominant systematic uncertainty comes from spectral variation of the particle background between the 10-12 keV (MOS)/12-14 keV (pn) energy range used to determine the scaling, and the 0.3-8 keV energy range used in the profiles. Read & Ponman (2003) investigated the spectral properties of the particle background and report the variance in the background level in several energy bands for a large number of *XMM-Newton* observations. Based on their calculations we estimate that the systematic uncertainty on the particle background level due to spectral variation is $\sim 24\%$ for the pn and $\sim 10\%$ for the MOS. The double-subtraction method used compensates almost exactly for any discrepancy between the "true" particle background level in a particular profile bin and the estimated level based on the FWC files due to this systematic uncertainty, because the "local" background level we determine will include any deviation in the particle background not accounted for by the scaling FWC component; however, because the vignetting correction in the local background differs slightly from that in the profile bins (by up to 20%) a small systematic effect can be introduced. This effect is negligible in most profile bins (including the outermost few bins with the lowest sur-

Table 3. Results from spectral analysis.

Region	power law		Apec		χ^2/dof
	Photon Index	Normalization (photons keV^{-1} cm^{-2} s^{-1})	T(keV)	Normalization (10^{14} cm^{-5})	
Lobes	$1.71^{+0.13}_{-0.17}$	$5.76^{+0.83}_{-1.54} \times 10^{-5}$	$1.36^{+0.39}_{-0.17}$	$5.98^{+5.82}_{-2.77} \times 10^{-5}$	1229/1049
Region 1	-	-	1.18 ± 0.11	$1.01^{+0.24}_{-0.25} \times 10^{-4}$	1146/1047
Region 2	-	-	$0.86^{+0.13}_{-0.05}$	$7.6 \pm 0.5 \times 10^{-5}$	862/623
Region 3	-	-	$1.72^{+0.9}_{-0.49}$	$4.56 \pm 1.23 \times 10^{-5}$	35/25

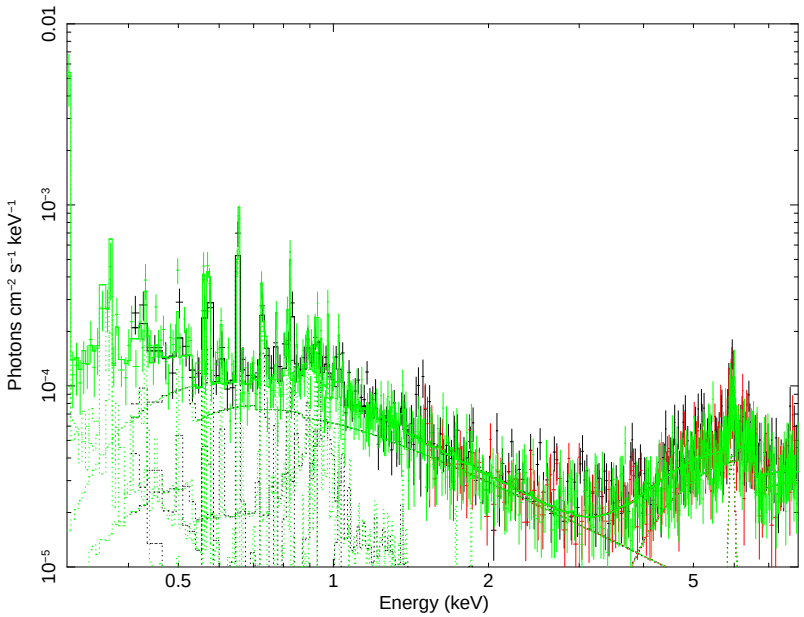

Figure 3. Unfolded spectrum for the AGN, lobes and environment after particle background subtraction. The value for the reduced χ^2 for the fit to this spectrum was 1.17. The iron Kα line at 6.4 keV is clearly visible in this plot. The green represents the PN data, the black is the MOS1 data and the red is the MOS2 data.

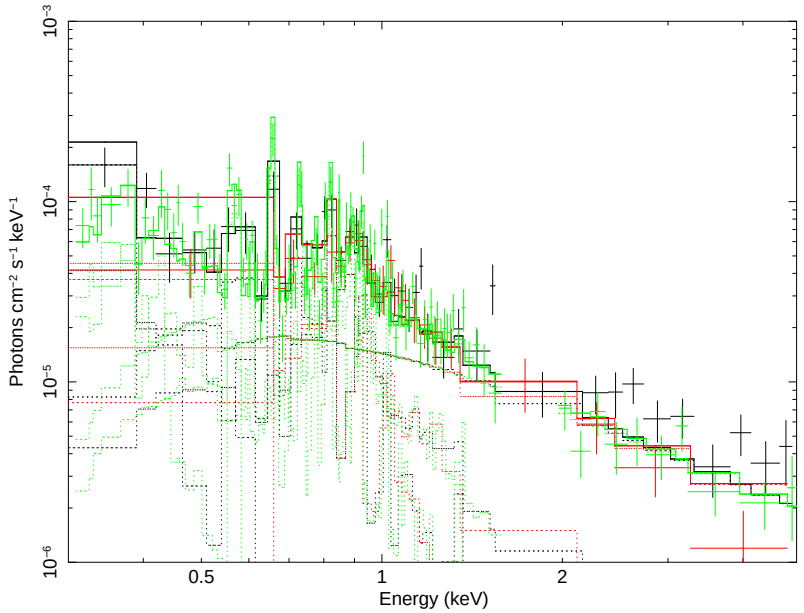

Figure 4. Unfolded spectrum for the outer region (region 4). This has been rebinned in XSPEC to clearly show the model components. We used an absorbed apec model for fitting the data as described in Section 3.3.3. The reduced χ^2 for the fit to this spectrum was 1.38. The green represents the PN data, the black is the MOS1 data and the red is the MOS2 data.

face brightness where the relative vignetting term is small), and always $< 5\%$ (pn) or $< 1\%$ (MOS). We therefore conclude that the reported statistical uncertainties on the surface brightness profile accurately reflect the true uncertainty.

4.2 Pressure

The dynamics of 3C 452 are determined by the relationship between the internal (lobe) and external (thermal) pressure as a function of position in the group.

To calculate the internal pressure we used SYNCH (Hardcastle et al. 1998a). SYNCH models inverse-Compton scattering of the CMB and synchrotron photons. The inputs to SYNCH are an electron energy spectrum, the geometry of the source region (we modelled the lobes as a cylinder with length (incorporating both lobes) 280 arcsec and radius 35 arcsec) and synchrotron flux density measurements (we used the 178-MHz data from the 3CRR catalogue and 1.4-GHz measurements from the image discussed in Section 2). The electron energy spectrum was a broken power law, with $\delta = 2$ at low energies steepening to 3 at high energies, γ_{min} to be 100,γ_{max} to be 10^8 and γ_{break} to be 6,000. SYNCH fits the electron spectrum to the radio observations and outputs an inverse-Compton prediction for a given magnetic field strength. The magnetic field strength is found by comparing the observed X-ray emission at 1 keV and the predicted X-ray inverse-Compton emission; we measure a lobe magnetic field strength of 0.175 ± 0.010 nT, significantly below the equipartition value of 0.52 nT. Assuming that only the relativistic electrons and the magnetic field contribute to the lobe pressure (Croston et al. 2004 have tested this assumption) then the electron spectrum and magnetic field strength give us a total energy density and internal pressure in the lobes. We found the internal pressure to be 2.6×10^{-13} Pa (the systematic uncertainties dominate over the statistical uncertainties and for this reason we present the internal lobe pressure without errors).

From the surface brightness profile and the measured temperature of the external gas we can find the external pressure at a given radius from the AGN, using the method of Birkinshaw & Worrall (1993). Fig. 6 shows the pressure as a function of radius. We see that the internal pressure is less than the external pressure at radii less than ~ 80 arcsec; thus the source should be contracting in its inner regions. Further out, though, the source is overpressured, and the difference is greatest at the far end of the lobes, where $p_{\rm int}/p_{\rm ext} = 2.4$, high enough that the source should be driving a shock into the external medium.

Projection affects both the size of the source (thus affecting the inferred internal pressure from the inverse-Compton measurements) and the environment in which it is embedded, so in general the effect of projection on measurements of internal to external pressure ratio is complicated (e.g. Hardcastle & Worrall 2000). In this particular case we expect that the source will be no more than 45° from the plane of the sky, since it is a narrow-line radio galaxy and the unification angle for these objects is of that order (e.g. Barthel 1989; Hardcastle et al. 1998b). Investigating different projection angles in the range $0^\circ < \theta < 45^\circ$, we find that although an increase in θ means a drop in internal pressure, as expected, it tends to increase the ratio between the internal and external pressures, up to a value of 3.2 at $\theta = 45^\circ$: so if anything the expected shock would be stronger, and our conclusions about the source dynamics are unchanged by plausible projection factors.

We discuss the implications of these results in Section 5.

5 DISCUSSION

5.1 AGN

The model that best fits our *XMM-Newton* data gives us an unabsorbed 0.5-10 keV luminosity for all components of the model of $(1.44^{+0.08}_{-0.07}) \times 10^{44}$ ergs s^{-1}. This is not directly comparable to the results of the *Chandra* analysis presented by Isobe et al. (2002) and Evans et al. (2006), since they used a slightly different model. To make a direct comparison and search for any evidence of AGN variability, we used the same extraction regions that we used for the AGN spectrum on the *Chandra* data used by Isobe et al. (2002) and Evans et al. (2006). We found the unabsorbed 0.5-10 keV luminosity for the *Chandra* AGN spectrum to be $(1.55^{+0.24}_{-0.19}) \times 10^{44}$ ergs s^{-1}. We directly compared key parameters of both datasets (e.g. the absorbed column density) and found that there were no significant differences between the *Chandra* and *XMM-Newton* data. This suggests that there has been very little variability in the 6 years between the observations using *Chandra* and *XMM-Newton*.

5.2 Lobes

Inverse-Compton emission from the lobes is clearly detected in our *XMM-Newton* data. Our flux density measurement (40 ± 4 nJy at 1 keV) is in excellent agreement with the results from *Chandra* data: Isobe et al. (2002) give 41 ± 15 nJy while Croston et al. (2005a) , in their analysis of the same data, quote 37 ± 2 nJy. Both previous analyses, like ours, fitted a combination of thermal and power-law models to the spectrum of the lobe region. The differences in the error bars presumably arises in part because Isobe et al. allowed the Galactic $N_{\rm H}$ to vary; we follow Croston et al. (2005b) in keeping it fixed. Our measurement of the photon index of the power-law component is also very consistent with the results of Croston et al. (2005a).

5.3 Environmental impact

We can make a rough estimate of the work done by the lobes on the environment. Modelling the lobes as a cylinder in the plane of the sky (as described above, Section 4.2) the total lobe volume is 1.15×10^{65} m^3. The energy stored in the lobes is then the energy density times the volume, or 9.1×10^{52} J. Roughly equating the work done on the environment with 1/3 of this, we obtain $PV \approx 3.0 \times 10^{52}$ J or 3.0×10^{59} ergs.

As we saw in Section 3.3.3, the outer regions of the host group are cooler by 0.32 ± 0.14 keV than the regions at radii comparable to the extent of the lobes. We can use our estimate of the PV work done by the lobes to ask whether this temperature difference is consistent with the idea that the radio source is heating the IGM in the inner part of the group.

Using the standard formulae for the proton number density in a β model and the relation between the number of electrons and the number of protons (e.g. Birkinshaw & Worrall 1993), we can calculate the thermal energy stored in a sphere of gas within the region that could plausibly have been affected by the radio source (region 1).

$$n_p = n_{p0} \left(1 + \frac{r^2}{r_{cx}^2}\right)^{\frac{-3\ \beta}{2}} \quad (1)$$

$$n_e = 1.18 n_p \quad (2)$$

where n_{p0} is the central proton number density which we obtain

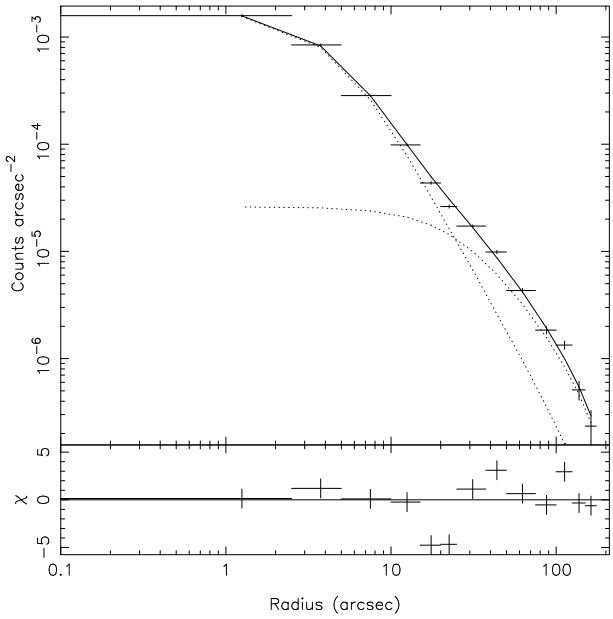

Figure 5. Surface brightness profile for 3C452 with the best fitting point source + β model which has $\beta = 0.53$ and core radius 21.98 arcsec.

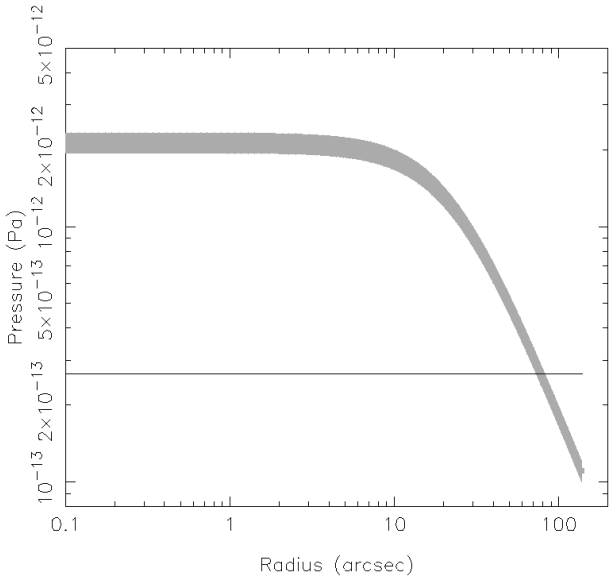

Figure 6. Pressure profile which shows the external pressure as a function of radius. The straight line across represents the internal pressure. Where the external pressure lies above the line, the lobes are contracting; below the line, the lobes are expanding.

from the pressure profile (Fig.6) , β and r_{cx} are the parameters of the β-model found by fitting to the surface brightness profile, and n_p and n_e are the proton and electron number densities at a given radius.

We then integrate equation 1 out to $r = 245$ kpc (160 arcsec) to determine the total number of particles in our sphere of influence, $N_{\rm tot} = 3.24^{+0.44}_{-1.07} \times 10^{68}$; multiplying this by $\frac{3}{2}kT$ (where T is the temperature of the gas in region 1 as found in the spectral extraction) gives the thermal energy stored in the region, $9.17^{+0.89}_{-2.93} \times 10^{52}$ J or $9.17^{+0.89}_{-2.93} \times 10^{59}$ erg. Effectively, this calculation also gives us the heat capacity of the gas in the region, on the assumption that all work done on the gas remains present as excess heat, $C = \frac{3}{2}kN_{\rm tot}$. Using this, we find that the work done by the AGN (as calculated above) should increase the temperature of the inner region by 0.39 keV. This is very consistent with the observed higher temperature in the centre of the group. There are several important caveats in doing this simple comparison: firstly, the estimate of PV work done is probably not accurate to within better than a factor of 2; secondly, we might expect that at least some of the work done by the radio source will go into lifting gas out of the centre of the group, i.e. into potential and not thermal energy; and thirdly, we do not know the original (undisturbed) temperature of the gas in region 1, and observations of groups and clusters show that the temperature profiles are unlikely to be flat (e.g. Pratt et al. 2007). However, it would obviously be possible for the estimate of AGN work done and the temperature difference to be grossly inconsistent (e.g. if the central temperature had been significantly less than the outer temperature) and this is not what we observe.

Finally, we note that the energy stored in the lobes is very comparable to the *total* thermal energy in region 1, and thus comparable to the gravitational binding energy of a significant fraction of the mass in the group. If the energy stored in the lobes is eventually thermalized, it will have a much more dramatic effect on the intra-group gas than the current work being done by the radio source.

5.4 Shock heating

Our results show that the ratio between the internal pressure and the external pressure is greater than 2 at the edge of the lobes. This suggests that the lobes should be expanding supersonically. We can estimate the temperature of the post-shocked gas in order to compare it to what is seen observationally. Using the Rankine-Hugoniot relationships, we can derive equations for the pressure and temperature in terms of the Mach number and the polytropic index. For the pressure,

$$\frac{P_2}{P_1} = \frac{2\Gamma M_1^2 + (1-\Gamma)}{\Gamma + 1} \tag{3}$$

where P_2 is 2.64×10^{-13} Pa (i.e. we assume that the post-shock pressure is equal to the lobe pressure), P_1 is 1.11×10^{-13} Pa (the external pressure) and Γ is $\frac{5}{3}$. Rearranging for M_1, we find that the Mach number is 1.6.

We can then determine the expected temperature using the relation between pre- and post-shock temperatures:

$$\frac{T_2}{T_1} = \frac{[2\Gamma M_1^2 + (1-\Gamma)][\Gamma - 1 + 2M_1^2]}{(\Gamma+1)^2} \tag{4}$$

where T_1 is 1.18 keV (pre-shocked gas temperature), Γ is $\frac{5}{3}$ and M_1 is 1.6. We find the post-shocked gas temperature (T_2) to be 1.94 keV. In Section 3.3.3, we found that the temperature in the region we defined at the edge of the lobes (region 3) was $1.72^{+0.9}_{-0.49}$ keV, which is at least consistent with the idea that the lobes are driving a shock of the expected strength into the IGM at their overpressured tips. However, there is no direct evidence for such a shock in the surface brightness profiles – unsurprisingly, since the density change in a weak shock like this is small. Much deeper observations will be needed to detect shocks around sources like 3C 452 if, as our modelling suggests, they are confined to the outer few tens of kpc of the lobes.

6 SUMMARY AND CONCLUSION

We have presented a deep *XMM-Newton* observation of the AGN, lobes and group environment of the nearby, powerful FRII radio galaxy 3C 452. This is the most sensitive X-ray observation of this source made so far and it has allowed us to measure the X-ray properties of the source more accurately than has previously been possible. We have compared the results from *XMM-Newton* with those derived from an earlier *Chandra* observation, and shown that there is very little variation in the AGN properties; there is no sign of variability in this object. Our data give an excellent detection of the inverse-Compton emission from the lobes; the flux density we measure is very consistent with earlier work. We have used our measurements of the properties of the group environment, possible for the first time with the *XMM-Newton* observations, to search for any large scale heating caused by the radio source in the environment of 3C 452. We measured the temperatures of three regions. Region 1 is a region with a radius of 160 arcsec, centred on the AGN with a temperature of 1.18 ± 0.11 keV. Region 2 has a radius of 320 arcsec, centered on the AGN with a temperature of $0.86^{+0.13}_{-0.05}$ keV. Finally, region 3 is a box of length 111 arcsec and width 70 arcsec intended to assess the temperature of any shock at the leading edge of the eastern lobe and a temperature of $1.72^{+0.89}_{-0.49}$ keV was found. Using the inverse-Compton detection of the lobes (40 ± 4 nJy), we have measured the internal lobe pressure, and from that have been able to estimate the work done by 3C 452 on its environment. If all of this work were put into heating the group-scale gas within a sphere defined by the size of the radio source, we would see an increase in temperature in the central regions of the group which is in fact very consistent with what we observe. Our pressure measurements (2.64×10^{-13} Pa for the internal pressure and 1.11×10^{-13} Pa for the external pressure (at the edge of the lobes)) also imply that the outer edges of the lobes are overpressured and driving a shock, while the inner parts of the lobes are underpressured and contracting; temperature measurements at the edge of the lobes are consistent with a shock model but our data are still not deep enough to claim a detection. Finally, we have shown that the total energy in the lobes is comparable to the thermal energy in the surrounding environment (the thermal energy stored in the lobes is $9.17^{+0.89}_{-2.93} \times 10^{52}$ J or $9.17^{+0.89}_{-2.93} \times 10^{59}$ erg), so that if the energy in the lobes is ever thermalized it will have a much bigger effect on the environment than the radio source is having at the present time.

ACKNOWLEDGEMENTS

DLS would like to thank friends and family for their unwavering support throughout this work. MJH would like to thank the Royal Society for a research fellowship.We would like to thank Etienne Pointecouteau, Monique Arnaud and Gabriel Pratt for developing the background calibration method used in this paper and for providing filter-wheel closed background datasets. This work is based on observations obtained with *XMM-Newton*, an ESA science mission with instruments and contributions directly funded by ESA Member States and the USA (NASA).

REFERENCES

Barthel, P. D. 1989, ApJ, 336, 606
Basson, J. F. & Alexander, P. 2003, MNRAS, 339, 353
Belsole, E., Worrall, D. M., Hardcastle, M. J., & Croston, J. H. 2007, MNRAS, 381, 1109
Birkinshaw, M. & Worrall, D. M. 1993, ApJ, 412, 568
Black, A. R. S., Baum, S. A., Leahy, J. P., et al. 1992, MNRAS, 256, 186
Croston, J. H., Birkinshaw, M., Hardcastle, M. J., & Worrall, D. M. 2004, MNRAS, 353, 879
Croston, J. H., Hardcastle, M. J., & Birkinshaw, M. 2005a, MNRAS, 357, 279
Croston, J. H., Hardcastle, M. J., Birkinshaw, M., Worrall, D. M., & Laing, R. A. 2008, MNRAS, 386, 1709
Croston, J. H., Hardcastle, M. J., Harris, D. E., et al. 2005b, ApJ, 626, 733
Evans, D. A., Worrall, D. M., Hardcastle, M. J., Kraft, R. P., & Birkinshaw, M. 2006, ApJ, 642, 96
Fanaroff, B. L. & Riley, J. M. 1974, MNRAS, 167, 31P
Feigelson, E. D., Laurent-Muehleisen, S. A., Kollgaard, R. I., & Fomalont, E. B. 1995, ApJL, 449, L149+
Goodger, J. L., Croston, J. H., & Hardcastle, M. J. 2011, MNRAS, submitted
Hardcastle, M. J., Alexander, P., Pooley, G. G., & Riley, J. M. 1998a, MNRAS, 296, 445
Hardcastle, M. J., Birkinshaw, M., Cameron, R. A., et al. 2002, ApJ, 581, 948
Hardcastle, M. J. & Croston, J. H. 2010, MNRAS, 404, 2018
Hardcastle, M. J., Croston, J. H., & Kraft, R. P. 2007a, ApJ, 669, 893
Hardcastle, M. J., Evans, D. A., & Croston, J. H. 2006, MNRAS, 370, 1893
Hardcastle, M. J., Evans, D. A., & Croston, J. H. 2007b, MNRAS, 376, 1849
Hardcastle, M. J. & Worrall, D. M. 2000, MNRAS, 319, 562
Hardcastle, M. J., Worrall, D. M., & Birkinshaw, M. 1998b, MNRAS, 296, 1098
Isobe, N., Tashiro, M., Makishima, K., et al. 2002, ApJL, 580, L111
Kataoka, J. & Stawarz, Ł. 2005, ApJ, 622, 797
Kraft, R. P., Birkinshaw, M., Hardcastle, M. J., et al. 2007, ApJ, 659, 1008
Lumb, D. H., Warwick, R. S., Page, M., & De Luca, A. 2002, A&A, 389, 93
Pratt, G. W., Böhringer, H., Croston, J. H., et al. 2007, A&A, 461, 71
Read, A. M. & Ponman, T. J. 2003, A&A, 409, 395
Scheuer, P. A. G. 1974, MNRAS, 166, 513
Tashiro, M., Kaneda, H., Makishima, K., et al. 1998, ApJ, 499, 713